Oscillation-induced displacement patterns in a two-dimensional porous medium: A lattice Boltzmann study

Olav Aursjø,* Henning Arendt Knudsen, Eirik G. Flekkøy, and Knut Jørgen Måløy
Department of Physics, University of Oslo, P.O. Box 1048, Blindern, NO-0316 Oslo, Norway
(Received 13 November 2009; revised manuscript received 13 April 2010; published 12 August 2010)

We present a numerical study of the statistical behavior of a two-phase flow in a two-dimensional porous medium subjected to an oscillatory acceleration transverse to the overall direction of flow. A viscous nonwetting fluid is injected into a porous medium filled with a more viscous wetting fluid. During the whole process sinusoidal oscillations of constant amplitude and frequency accelerates the porous medium sideways, perpendicular to the overall direction of flow. The invasion process displays a transient behavior where the saturation of the defending fluid decreases, before it enters a state of irreducible wetting fluid saturation, where there is no net transport of defending fluid toward the outlet of the system. In this state the distribution of sizes of the remaining clusters are observed to obey a power law with an exponential cutoff. The cutoff cluster size is found to be determined by the flow and oscillatory stimulation parameters. This cutoff size is also shown to be directly related to the extracted amount of defending fluid. Specifically, the results show that the oscillatory acceleration of the system leads to potentially a large increase in extracted wetting fluid.

DOI: 10.1103/PhysRevE.82.026305 PACS number(s): 47.56.+r, 47.55.df, 47.11.−j, 89.75.Da

I. INTRODUCTION

In the petroleum industry the search for ways to recover a larger volume fraction of the oil trapped in the reservoir rock is of great interest. In a reservoir where production is found uneconomical, residual oil patches may typically amount to a volume fraction of about 30%–40% or more. The last 60 years it has been reported on several occasions that oil fields experiencing earthquakes have observed a rise in the oil production both during and after such seismic activity [1]. This has provided a scientific interest in seismic stimulation of reservoirs as a possible method for enhanced oil recovery. A number of analytic as well as numerical descriptions of how a single oil droplet, stuck in a pore cavity may be mobilized by vibrations of the pore walls, have been produced over the last decade [2–7]. In these studies, vibrational frequencies both higher and lower than the characteristic Biot frequency [8–10] of the examined systems were investigated. In the high-frequency regime inertia effects dominate the dynamics, and effects such as resonance of the fluid-fluid interfaces of the stuck droplet were observed to occur [7]. In the low-frequency regime, on the other hand, viscous forces balance the applied forces and give an overdamped flow regime.

On a larger scale, Pride *et al.* numerically studied the influence of seismic stimulation on a set of oil droplets stuck in 10×10 pores flow cells and compared the results to an analytical set of criteria for successful mobilization of stuck droplets [11]. Some laboratory experiments with vibrational stimulation have also been produced [12–16]. Mainly these studies show how vibrations of a porous medium affect the saturation levels and production rates of the fluids therein. Among these, both experiments where the porous medium containing trapped residual fluid ganglia underwent stimulation [12–14] and experiments where the vibrational stimulation was applied during the whole invasion process [15,16] were conducted.

In the following we present a numerical study of the effect of applying an oscillatory force to a two-dimensional drainage process in a rigid porous flow cell. We have here kept the investigation to the overdamped flow regime, by keeping the frequency of the oscillatory stimulation lower than the characteristic Biot frequency of the system. In the simulations we used a two-dimensional (2D) lattice Boltzmann (LB) method [17–20]. By specifically investigating a two-dimensional system we have been able to simulate a larger system than computationally possible in a three-dimensional case. Contrary to previous LB studies, the relatively large system size allows us to study the statistical behavior of the pattern formation of the defending fluid rather than just local effects.

Displacement pattern formations in immiscible multiphase flow processes have been the focus of a vast number of studies, see [21–27] for references. Lately some studies have been done on the description of patterns and flow properties in steady-state two-phase flow [28–32]. But to a large extent, the experimental and theoretical work done on complex fluid patterns in porous media concern invasion processes determined by the dynamics of the invasion front alone. In drainage processes, it has been shown the existence of typically three such displacement structures [33]; capillary fingering [27,34] modeled by invasion percolation (IP) [35–37], fractal viscous fingering [25,38–42] modeled by diffusion limited aggregation (DLA) [38,40], and stable front displacement [43,44] modeled by anti-DLA [38]. The structures, however, in the transitional regimes between these three displacement regimes are not necessarily solely controlled by the behavior of the front. The final pattern formation may here also be strongly dependent on the cluster dynamics behind the front [45–47].

The invasion processes we have studied, are mainly in a regime where cluster dynamics behind the front is present. We have here therefore focused our investigation to the final irreducible displacement patterns, produced by the oscillatory stimulation of the system. These patterns consist of the

*olav.aursjo@fys.uio.no

 ©2010 The American Physical Society

defending fluid clusters/droplets left in the porous medium when there is no net transport of this fluid toward the outlet of the system. During the examination of the system, a large variety of the parameter combinations that control the fluid flow was probed. However, the principal purpose of the investigation was to explore the effects of the amplitude and the frequency of the oscillatory body force in such a system. In the state of irreducible wetting fluid saturation, the cluster size distribution of the remaining clusters are found to obey a power law with an exponential cutoff. The cutoff cluster size is directly determined by the flow and oscillatory stimulation parameters. A resulting collapse of the cluster size distributions for the parameter configurations probed reveals a scaling relation spanning over almost 4 orders of magnitude in cluster size. It is also found that the end saturation of the defending fluid is a function of the cutoff cluster size.

To impose a constant fluid flux in our otherwise well established LB method, a control loop feedback algorithm was developed. This algorithm is presented in Sec. III. The rest of the present article is organized as follows. First the numerical method is introduced in Sec. II. A description of our specific system is then given in Sec. III. This is followed by the numerical results in Sec. IV. This section is divided into a qualitative description of the transient invasion process and a statistical analysis of the final displacement patterns produced. A theoretical argument for having the cutoff cluster size observed is given in Sec. V. Section VI contains the concluding remarks.

II. NUMERICAL METHOD

The model we use in the LB simulations is a $D2Q6$ two-component lattice Bhatnagar-Gross-Krook (LBGK) algorithm, where we introduce surface tension in accordance with the method of Gunstensen *et al.* [18]. In this method particle density, particle flux density and concentrations are conserved on each lattice site. The component distributions $N_i^{\mathrm{R}}(\mathbf{x},t)$ and $N_i^{\mathrm{B}}(\mathbf{x},t)$ give the particle number and number flux densities of the two fluids (red and blue), i.e.,

$$\rho_{\mathrm{R,B}}(\mathbf{x},t) = \sum_i N_i^{\mathrm{R,B}}(\mathbf{x},t), \tag{1}$$

$$\rho_{\mathrm{R,B}}(\mathbf{x},t)\mathbf{u}^{\mathrm{R,B}}(\mathbf{x},t) = \sum_i N_i^{\mathrm{R,B}}(\mathbf{x},t)\mathbf{c}_i. \tag{2}$$

Here $\mathbf{u}^{\mathrm{R}}(\mathbf{x},t)$ and $\mathbf{u}^{\mathrm{B}}(\mathbf{x},t)$ are the velocities of the red and the blue component, respectively, in the position $\mathbf{x}$ at the time t. The set of vectors $\{\mathbf{c}_i; i=1,\ldots,6\}$ is the displacement vectors to the six nearest-neighboring sites. The distance between lattice sites, $|\mathbf{c}_i|$, is equal unity on an hexagonal lattice. The time step and lattice unit are set to unity. The two distribution functions contribute to a total population distribution $N_i(\mathbf{x},t)=N_i^{\mathrm{R}}(\mathbf{x},t)+N_i^{\mathrm{B}}(\mathbf{x},t)$ and a total density $\rho_N(\mathbf{x},t)=\rho_{\mathrm{R}}(\mathbf{x},t)+\rho_{\mathrm{B}}(\mathbf{x},t)$ that are used in the interaction equation

$$N_i'(\mathbf{x},t) = N_i(\mathbf{x},t) + \lambda(\mathbf{x},t)[N_i(\mathbf{x},t) - N_i^{\mathrm{eq}}(\rho_N,\mathbf{u})] + \frac{1}{3}\mathbf{F}(\mathbf{x},t)\cdot\mathbf{c}_i + \Phi_i(\mathbf{x},t). \tag{3}$$

Here, $-\lambda(\mathbf{x},t)$ is the inverse of the effective relaxation time and is given by

$$\lambda(\mathbf{x},t) = \frac{\lambda_{\mathrm{R}}\rho_{\mathrm{R}}(\mathbf{x},t) + \lambda_{\mathrm{B}}\rho_{\mathrm{B}}(\mathbf{x},t)}{\rho_{\mathrm{R}}(\mathbf{x},t) + \rho_{\mathrm{B}}(\mathbf{x},t)},$$

where the inverse relaxation times of the individual components, $-\lambda_{\mathrm{R}}$ and $-\lambda_{\mathrm{B}}$, are related to the kinematic viscosities of the respective fluids by

$$\nu_{\mathrm{R,B}} = -\frac{1}{4}\left(\frac{1}{2} + \frac{1}{\lambda_{\mathrm{R,B}}}\right). \tag{4}$$

The $\mathbf{F}(\mathbf{x},t)$ represents all external body forces in the system of interest.

We have chosen the equilibrium distribution in Eq. (3) to be

$$N_i^{\mathrm{eq}}(\rho_N,\mathbf{u}) = \frac{\rho_N}{6}(1 + 2\mathbf{u}\cdot\mathbf{c}_i + 4(\mathbf{u}\cdot\mathbf{c}_i)^2 - 2|\mathbf{u}|^2), \tag{5}$$

where $\mathbf{u}=(\rho_{\mathrm{R}}\mathbf{u}^{\mathrm{R}}+\rho_{\mathrm{B}}\mathbf{u}^{\mathrm{B}})/\rho_N$ is the velocity, in the position $\mathbf{x}$ at the time t, of the two components combined. With this choice the incompressible Navier-Stokes equations,

$$\nabla\cdot\mathbf{u} = 0, \tag{6}$$

$$\frac{\partial\mathbf{u}}{\partial t} + (\mathbf{u}\cdot\nabla)\mathbf{u} = -\frac{1}{\rho_N}\nabla p + \nu\nabla^2\mathbf{u} + \frac{1}{\rho_N}\mathbf{F}, \tag{7}$$

are recovered in the long-wavelength, low-Mach-number limit. The term $\Phi_i(\mathbf{x},t)$ in Eq. (3) is a particle density and particle flux density conserving perturbation term that creates a macroscopic interface tension between the two fluids. This term is given as

$$\Phi_i(\mathbf{x},t) = A|\mathbf{f}(\mathbf{x},t)|\left[\frac{(\mathbf{c}_i\cdot\mathbf{f})^2}{\mathbf{f}\cdot\mathbf{f}} - \frac{1}{2}\right], \tag{8}$$

where A is a parameter directly related to the interface tension, $\gamma=-9A\rho_0/\lambda$ [20]. Here, ρ_0 is the initial particle number density of the system. The vector $\mathbf{f}$ is the local fluid component gradient

$$\mathbf{f}(\mathbf{x},t) = \sum_i [\rho_{\mathrm{R}}(\mathbf{x}+\mathbf{c}_i,t) - \rho_{\mathrm{B}}(\mathbf{x}+\mathbf{c}_i,t)]\mathbf{c}_i. \tag{9}$$

The component distributions $N_i'^{\mathrm{R}}(\mathbf{x},t)$ and $N_i'^{\mathrm{B}}(\mathbf{x},t)$ are found by maximizing $\Sigma_i(N_i'^{\mathrm{R}}(\mathbf{x},t)-N_i'^{\mathrm{B}}(\mathbf{x},t))\mathbf{c}_i\cdot\mathbf{f}$ in such a fashion that we have local conservation of the individual particle densities of the two components, as well as local conservation of the total population distributed in each direction. The component distributions for the next time step are

$$N_i^{\mathrm{R,B}}(\mathbf{x}+\mathbf{c}_i,t+1) = N_i'^{\mathrm{R,B}}(\mathbf{x},t), \tag{10}$$

where the time t is measured in number of time steps. Combined with Eq. (3) this equation is just a discretized approximation to the Boltzmann transport equation. This method

produces sharp interfaces between the two components.

Solid wall boundaries are implemented by a simple bounce-back rule, $N_i'(\mathbf{x},t)=N_{i+3}(\mathbf{x},t)$, that replaces the ordinary interaction equation at the wall sites [20]. The wetting properties of the walls are modeled by modifying $\mathbf{f}$ at sites neighboring the wall sites [48]. At these sites the neighboring density difference, $\rho_R(\mathbf{x}+\mathbf{c}_i,t)-\rho_B(\mathbf{x}+\mathbf{c}_i,t)$, is replaced by $\Delta\rho_{wall}=\rho_0 \cos\theta_w$, if position $\mathbf{x}+\mathbf{c}_i$ is a wall site. This expression introduces a static contact angle θ_w. A contact angle $\theta_w=0°$ gives a surface perfectly wet by the red fluid, while $\theta_w=180°$ makes the blue fluid perfectly wetting.

Injection of blue fluid into a system filled with a red fluid is simulated by letting the boundaries perpendicular to the flow be periodic to the total population distribution N_i, but also impose a recoloring so that all incoming populations on the injection side be blue while all incoming populations on the opposite boundary be red. To avoid creation of interface tension at the recoloration boundaries, the local fluid component gradient $\mathbf{f}$ of Eq. (9) is at these sites set to zero.

In our LB algorithm we have in the separate phases particle densities $\rho_{R,B}$ that are the same for the two components. If we let our frame of reference be defined by the porous medium, an inertial mass density difference between the fluids may, in a regime of low Reynolds numbers, be introduced through a body force that differentiate between the two fluid components. The chosen inertial density difference determines then the forcing level on each phase. This will give any desired buoyancy effects. Note that our frame of reference is then an accelerated one.

III. SYSTEM

The process we have studied is an invasion process with incompressible fluids, where a less viscous, nonwetting fluid invades a porous medium occupied by a more viscous, wetting fluid. However, while draining, the system is subjected to a time dependent oscillatory acceleration.

At all times there is a background force that drives the fluid through the model. We define our coordinate system such that this background flow is along the x axis, while the y axis is perpendicular to that flow, see Fig. 1. The inlet is then defined to be at $x=0$ and the outlet at $x=L$, where L is the length of the system. Properties of the porous medium and the fluids are given in lattice units in Table I.

The invasion process may in the simulations be driven in two alternative ways, either by a global body force, constant in time, throughout the system, or a constant particle flux boundary condition. In LB simulations it is convenient to let a flow be driven by a body force. The constant flux is therefore maintained by a body force $F_x(t)$ acting globally on the whole system. This also minimizes the compressibility effects inherent in our LB algorithm. The flux controlling body force varies with time as

$$\frac{\partial F_x(t)}{\partial t} = K_P[J_0 - J_x(t)] - K_D\frac{\partial J_x(t)}{\partial t}. \tag{11}$$

Here, J_0 is the desired particle flux density and $J_x(t)$ is the mean particle flux density measured in the system at a time t. K_P and K_D are positive tuning parameters that determine the response of the body force. This is basically a control loop feedback mechanism that tries to correct the error between the measured $J_x(t)$ and the desired J_0. The second term in the expression is proportional to the rate of change in the measured particle flux density and is introduced to keep the fluctuations in $J_x(t)$ to a minimum. Without this derivative term the measured flux density will typically exhibit large oscillations around J_0 and never stabilize.

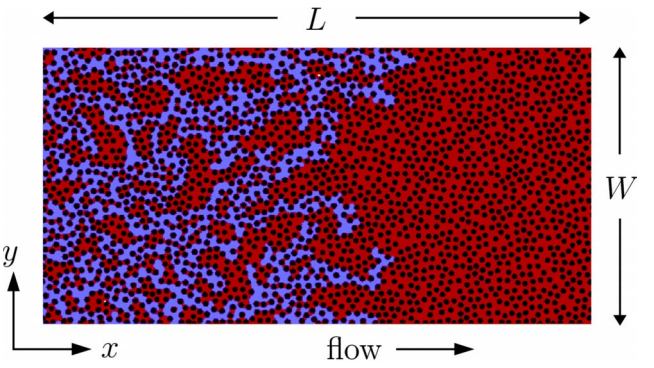

FIG. 1. (Color online) Schematic representation of the flow system. A blue (light gray) nonwetting fluid invades a red (dark gray) wetting fluid through a black porous medium. The invasion is here driven from left to right by a globally constant body force and is not under the influence of any oscillatory acceleration.

In our simulations $K_P=1.0$ and $K_D=0.5$ gave the most stable flux. When we used this flux controlling body force, the maximal deviation from the desired flux density was observed to be less than 1.5%. Figure 2 shows the time evolution of the flux density $J_x(t)$ in two particular simulations. The black line shows the variations in $J_x(t)$ when the flux controlling force is the only external forcing to the system, while the light gray line indicates the behavior when the system in addition is subjected to another external force. This additional force is equal to the strongest external stimulation of the system simulated in this study. This shows that when the control loop feedback mechanism has to take into account other strong external forces, the measured flux deviates more from the desired value.

TABLE I. Geometrical parameters and fluid properties in the lattice Boltzmann system. All quantities are given in lattice units and unit time.

Description	Symbol	Value
Model length	L	800
Model width	W	400
Obstacle diameter	b	8
Porosity	ϕ	0.67
One-phase permeability	κ	1.0
Contact angle	θ_w	10°
Wetting fluid (red) viscosity	ν_w	0.1
Nonwetting fluid (blue) viscosity	ν_{nw}	0.02
Initial particle number density	ρ_0	3.0
Surface tension	γ	0.05–0.3

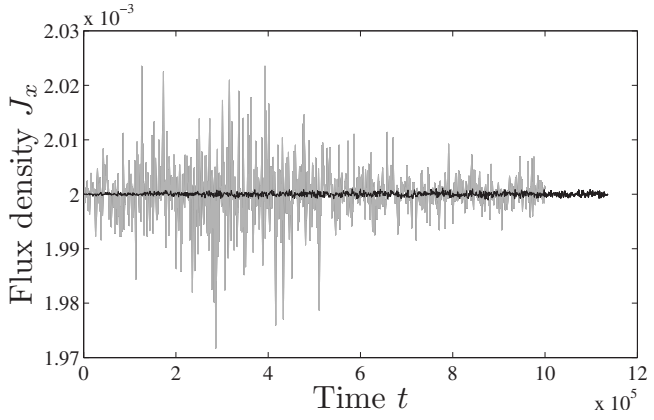

FIG. 2. The time evolution of the particle flux density in a system subjected to the flux controlling body force presented in Eq. (11). The black line shows the typical system behavior when the flux controller is the only external force. The light gray line shows the behavior when another additional strong external force is introduced to the system. The particle flux density and the time are measured in lattice units.

A global body force $F_x(t)$, as we have, gives a flow equivalent to an experimental setup where the flow is driven by a constant external pressure gradient $\partial_x p_{\text{exp}} = -F_x(t)$ across the system. The only differences are in the pressure measurements. At an arbitrary position (x,y) in the system, the relation between the pressure p_{LB} in the simulations and the experimentally achieved pressure p_{exp} is therefore given as

$$p_{\text{exp}}(x,y,t) = p_{\text{LB}}(x,y,t) + F_x(t)(L-x). \tag{12}$$

When we refer to pressure in this paper we refer to the pressure p_{LB} measured in the simulations.

The porous medium itself is made up of circular disks, with a diameter $b=8$ lattice units. These are distributed over the system such that none of the disks overlap or touch. The spacing between the disks constitutes the approximately 60×30 pores in the system. Although this means the number of lattice sites in a single pore throat is small, it is enough to reproduce fluid behavior within each pore throat [49]. To minimize boundary effects at the sides parallel to the background flow, the system is periodic in the direction perpendicular to this flow.

While draining the pore space the porous medium is subjected to an oscillatory acceleration with a sinusoidal time dependence. In our system, where we have chosen the porous medium as the frame of reference, this is, in accordance with the equivalence principle, observed as an oppositely directed body force proportional to the external acceleration and the inertial mass density of the fluid. This body force may be expressed as

$$\mathbf{F}_a(\mathbf{x},t) = \rho(\mathbf{x},t)\mathbf{a}\,\sin(2\pi t/T), \tag{13}$$

where $\rho(\mathbf{x},t)$ is the mass density of the fluid, $a=|\mathbf{a}|$ is the absolute value of the acceleration amplitude and T is the oscillation period. Consequently, the vector $\mathbf{a}$ points here in the opposite direction of the external acceleration of the porous medium. Numerically, the mass density of the defending wetting fluid is always kept equal to $\rho_{\text{R}}(\mathbf{x},t)$ defined in Sec. II, while the mass density of the invading nonwetting fluid is given by $(\rho_{nw}/\rho_w)\rho_{\text{B}}(\mathbf{x},t)$. Here ρ_{nw}/ρ_w is the mass density ratio between the fluids we want to simulate.

Since our fluids are accelerated relative to the surrounding porous medium, by a body force proportional to the mass densities of the fluids, the effects of the acceleration may be divided into two separate effects. First, we may get a mean flow relative to the porous medium and, additionally, we may get a relative flow between the two fluid phases caused by different mass densities, i.e., a buoyancy effect. Constant flux boundary conditions (including solid walls) in the direction of the oscillations, would only allow us to study the buoyancy effects alone. The acceleration of the system would in this case not contribute to the mean flow, since this would by definition already be fixed. We have here instead chosen to study the combined effect. This also minimizes potential compressibility effects in our LB system. In order to study the combined effect of the acceleration in both the constant flux driven simulations and the simulations with a global body force, constant in space and time, we apply the oscillatory body force perpendicular to the direction of the background flow, i.e., along the y axis (see Fig. 1). Due to our periodic boundary conditions in this direction, both a flow relative to the porous medium and a relative flow between the fluids will affect the dynamics of the process.

The invading fluid in the simulations is of finite viscosity, therefore the flow around fluid clusters left behind the invasion front, will give rise to a viscous pressure drop across them. The structure of clusters behind the front is then not left static immediately after they have been disconnected from the front. Consequently, the simulations were run for well beyond breakthrough, i.e., the drainage of the system continued after the most advanced part of the nonwetting fluid had penetrated through the whole length of the porous medium. The simulations were kept running until no more wetting fluid could be drained from the medium.

IV. RESULTS

In order to compare the results from the lattice Boltzmann simulations to other results it is convenient to construct a set of dimensionless numbers that characterize the physical behavior. Any two systems will have the same fluid behavior if the values of the dimensionless numbers are the same. Along with the viscosity ratio of the invading fluid to the defending fluid, the mass density ratio, the capillary number, and the Reynolds number, we introduce two additional numbers. The first of these is the ratio of oscillatory body force to background body force and the other is the oscillation period T relative to the one-phase invasion time of one pore given a background body force F_x. These are thus given as

$$\hat{F}_a = \frac{\rho_w a}{F_x} \quad \text{and} \quad \hat{Q} = \frac{\kappa F_x}{\mu_w \phi b} T, \tag{14}$$

where we have used Darcy's law to establish the latter expression. Here, κ is the one-phase permeability of the porous medium, ϕ is the porosity, and b is the characteristic length

scale of the pore. The dimensionless $\hat{Q}$ may also be viewed as the average number of pores, in the x direction a wetting fluid element in a one-phase flow propagates through, in one period of oscillation, having a background body force F_x.

The use of Darcy's law is valid only in a state where the viscous forces have had time to balance the applied forcing of the flow. To ensure that our system is in this overdamped flow regime, it is sufficient to check that the fluid velocity is close to being in phase with the applied oscillatory body force. For all the frequencies used in this study there are no observable phase shift between the applied body force and the measured fluid velocity. We therefore conclude that the frequencies are all in the low frequency regime and well below the characteristic Biot frequency of the system [10]. If flow velocity is not an observable/measurable quantity, a rough estimate for the time scale giving fully developed viscous flow during oscillations can be found by considering the oscillating fluid flow between two horizontal plates [9,50]. The analytical solution for the fluid motion implies that the velocity field, oscillating in time, will be in phase with the applied body force if $T \gg \pi h^2/\nu$, where T is the period of the oscillations, h is the plate separation, and ν is the kinematic fluid viscosity.

We have chosen to define a capillary number of the background flow on pore scale [44], using Darcy's law, as

$$\mathrm{Ca}_x = \frac{(\Delta p)_{\mathrm{viscous}}}{(\Delta p)_{\mathrm{capillary}}} = \frac{b^2 F_x}{\gamma}. \tag{15}$$

Since the processes driven by constant mass flux boundary conditions experience a changing background body force during the invasion we have, in our definitions of the dimensionless numbers, chosen to use the body force F_x obtained when no more wetting fluid is drained from the system.

The simulations have an estimated background flow capillary number $\mathrm{Ca}_x \sim 10^{-2}-10^{-1}$. Since this number does not take into account the effect of the transversal acceleration of the system, it does not necessarily describe what kind of flow regime the system is in. To classify the flow regime $(\hat{F}_a^2+1)^{1/2}\mathrm{Ca}_x$ is a more suitable number, since this corresponds to the total force imposed on the system. In the simulations this number has a range of $10^{-2}-10$ approximately, showing that the speed of the fluid front displacement differs by three orders of magnitude through our set of simulations.

The defined set of dimensionless numbers and their respective range of values in our simulations are presented in Table II. In each simulation these numbers are fixed. During this investigation the main objective was to study the effects of the frequency and amplitude of the oscillatory body force. To do this, the simulations were divided into sets where the oscillatory body force amplitude were varied, while all other parameters were kept constant. 17 such sets of simulations were produced. The number of simulations in each set ranged from 4 to 17. In all, 139 different parameter configurations were probed.

TABLE II. The set of dimensionless numbers that characterize the physical behavior of our process.

Description	Symbol	Expression	Value
Porosity	ϕ		0.67
Contact angle	θ_w		10°
Viscosity ratio	M	μ_{nw}/μ_w	0.2
Mass density ratio		ρ_{nw}/ρ_w	$10^{-3}-1$
Cap. no, bg flow	Ca_x	b^2F_x/γ	$10^{-2}-10^{-1}$
Reynolds number	Re	$b\bar{u}/\nu_{nw}$	$10^{-2}-1$
# pores invaded in T	$\hat{Q}$	$\kappa F_x T/(\mu_w \phi b)$	$10^{-1}-20$
Body force ratio	$\hat{F}_a$	$\rho_w a/F_x$	$10^{-1}-10^{2}$

A. Transient behavior

The initial transient behavior of the system demonstrates a number of interesting features. Since this paper focuses on the behavior of the system after it has reached a state of irreducible wetting fluid saturation, their nature will only be described briefly and qualitatively. Figure 3 shows a comparison of the transient regime in two systems with the same background capillary number, with and without any oscillatory acceleration. In the pure drainage process not subjected to any oscillatory stimulation, where the nonwetting fluid displaces the wetting defender, an invasion front is observed to propagate through the system, see left column of Fig. 3. The width of this front grows until a part of the defending fluid detaches from the front and creates a separate cluster. The front propagation continues until it reaches the outlet. At the lowest capillary numbers, the flow shows a front behavior and a displacement structure that closely resembles capillary fingering. Faster invasion gives a more compact flow. And the invaded structure is seen to become denser with increasing displacement speeds [45–47]. Fractal viscous fingering [39,40] is not observed, due to the finite viscosity ratio $M=0.2$ in the simulations. Another characteristic feature of this flow regime is that clusters above a certain size, already separated from the front during the invasion, can continue to move after detachment. Since the invading fluid is of finite viscosity, a viscous pressure drop across the detached clusters, will allow clusters that are large enough to overcome the capillary forces and continue toward the outlet.

The behavior described above is also observed in the simulations when the system is subjected to a transverse oscillatory acceleration, see right column of Fig. 3. In addition to these features, the oscillatory stimulation will, if the acceleration amplitude and oscillation period are large enough, cause individual fingers in the front to snap off and create nonwetting clusters in front of the connected displacement front. This results in a smaller front width and therefore also smaller defending fluid clusters left behind, detached from the advancing front. This means that the initial invasion process is prolonged and the invasion front uses more time to reach the outlet. It is also observed that the shaking could move a cluster of defending fluid through pores otherwise inaccessible. Depending on the cluster configuration this could lead to coalescence with other clusters, or the cluster could just fragment. If the clusters coalesce, they become more mobile and may more easily be transported toward the outlet. If they instead are fragmented into smaller pieces these become more immobile and harder to move. We ob-

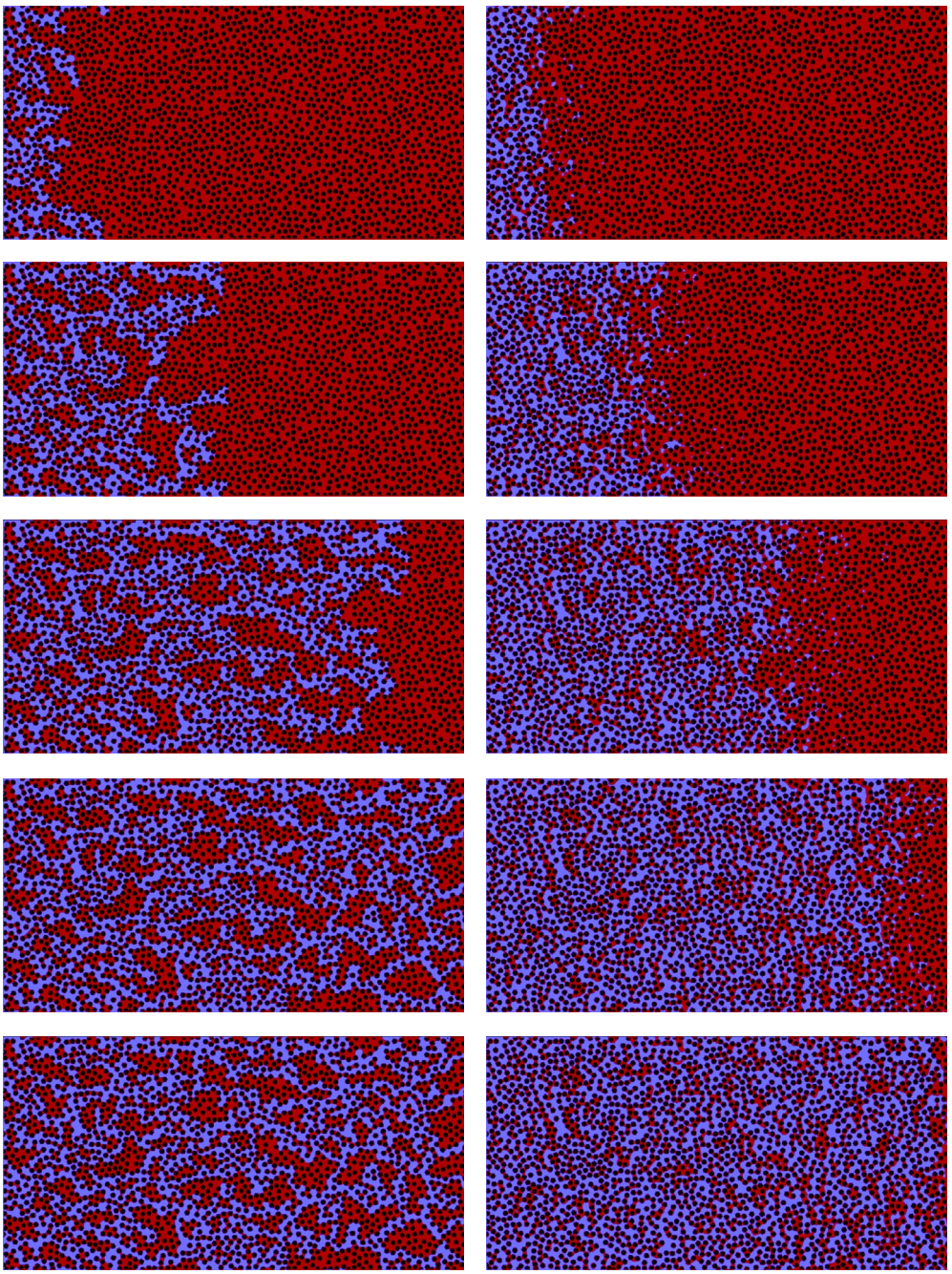

FIG. 3. (Color online) For background capillary number $\mathrm{Ca}_x = 1.9 \times 10^{-1}$, two invasion processes with and without transverse oscillatory stimulation are compared at different times in the transient regime. In both processes the invasion is driven from left to right by a body force constant in time and space, and the inertial mass density ratio is $\rho_{nw}/\rho_w = 10^{-3}$. The right column shows a system subjected to an additional oscillatory acceleration, transverse to the background flow, with stimulation numbers $\hat{F}_a = 20$ and $\hat{Q} = 1.89$. See Fig. 1 for color explanations.

serve that for some time after the initial invasion process there are more clusters coalescing than fragmenting, leading to a net transport of defending fluid out of the system. But as the concentration of these clusters decreases the fragmentation after a while balances the coalescence of clusters and it reaches a state of irreducible wetting fluid saturation with just as much coalescence as fragmentation, and no more net transport of defending fluid out of the system is measured.

B. State of irreducible wetting fluid saturation

After the initial transient behavior the system reaches a state where no more wetting fluid moves in the direction of the outlet, and a state of irreducible wetting fluid saturation has been established. Even though the defending wetting fluid has no net flux toward the outlet, the clusters may still be mobile in the transverse direction. The average of this flux of the defending fluid in the y direction, however, taken over

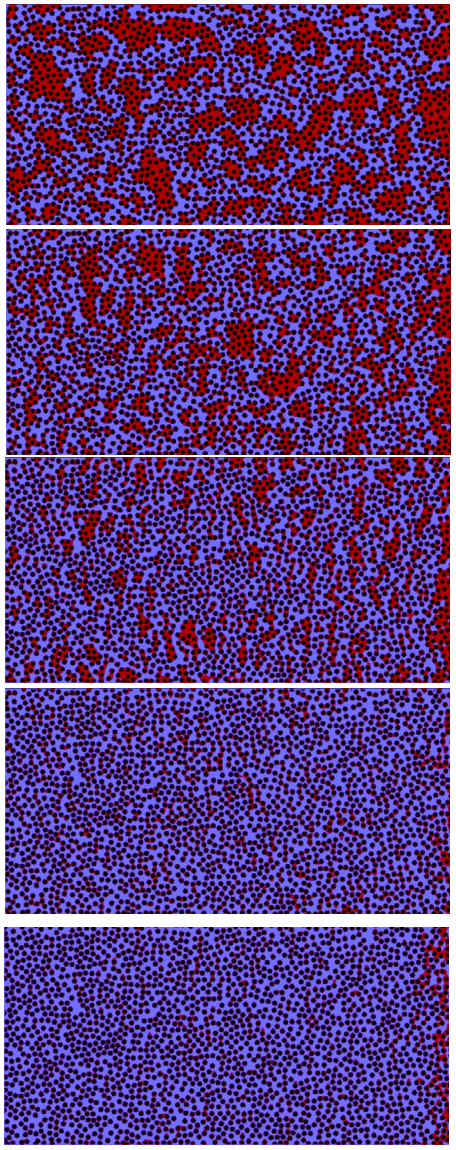

FIG. 4. (Color online) The five cluster configurations of irreducible saturation achieved with the combinations of dimensionless numbers presented in Table III resulting in the cluster distributions in Fig. 5. The systems are presented as in the table, with decreasing wetting saturation starting from the top. See Fig. 1 for color explanations.

one period, is also vanishing. In this state we analyzed the size/area distribution of the remaining wetting clusters. The porous system is undeniably relatively small, but proves big enough to give adequate statistics.

Figure 4 shows five configurations of wetting fluid clusters in a state of irreducible saturation, established under the influence of different flow and stimulation parameters. The dimensionless numbers for these simulations are given in Table III. These simulations specifically, are chosen to illustrate the span of cluster configurations we observe. The normalized cluster size distributions, i.e., the probability distributions, $P(s)$ as functions of the cluster size/area s divided by the pore length squared, extracted from each of these five simulations, are shown in the inset of Fig. 5. From the cluster configurations in Fig. 4 we observe that, due to boundary

TABLE III. Values of the dimensionless numbers defining the behavior of the cluster configurations displayed in Fig. 4.

Graph no.	Ca_x	$\hat{F}_a$	$\hat{Q}$	ρ_{nw}/ρ_w
◇ 1	1.4×10^{-1}	0		10^{-3}
▷ 2	8.0×10^{-2}	24	0.79	10^{-3}
◁ 3	1.5×10^{-1}	19	0.76	1
● 4	2.3×10^{-1}	32	2.3	10^{-3}
○ 5	1.0×10^{-1}	126	2.0	10^{-3}

effects, there are larger clusters located in a region close to the outlet. A region, of approximately 1/6 of the system size, adjacent to the outlet was therefore omitted when extracting the cluster size distributions. The full set of cluster size distributions from our simulations is presented in Fig. 6.

If we, as in percolation theory [51], assume that the normalized cluster size distribution behaves as

$$P(s) \propto s^{-\tau} \exp(-s/s^*), \tag{16}$$

we may define a statistical cutoff cluster size s^* for each of the individual distributions. This cutoff size determines the point where an exponential tail becomes dominant over the power law behavior in the distribution of cluster sizes. In addition, our system introduces a lower cutoff in the size distributions, where the cluster sizes are smaller than the size of a pore throat. At this point the distributions have been truncated. In a similar manner, the system size sets an absolute upper limit for the sizes of clusters possible to observe, i.e., an upper cutoff in the size distributions.

From the inset of Fig. 5 we observe that, starting with a distribution indicating a pure power law dependency (sym-

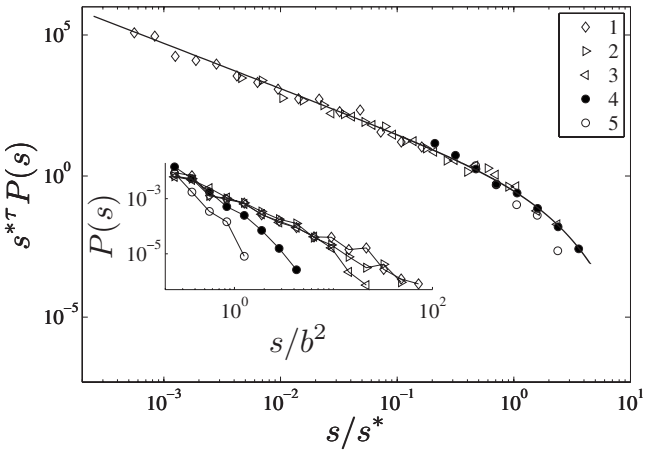

FIG. 5. Wetting cluster size distribution $P(s)$ in a state of irreducible saturation. The inset shows the cluster size distributions $P(s)$, extracted from the cluster configurations in the five simulations presented in Fig. 4, plotted against cluster size s divided by the pore length squared. The graphs are numbered with decreasing cutoff size s^*. In the main graph the horizontal and vertical axis are re-scaled with $1/s^*$ and $s^{*\tau}$, respectively, to give a data collapse. The power law exponent $\tau=1.6$. The solid line through the collapsed data sets is proportional to $(s/s^*)^{-1.6}\exp(s/s^*)$.

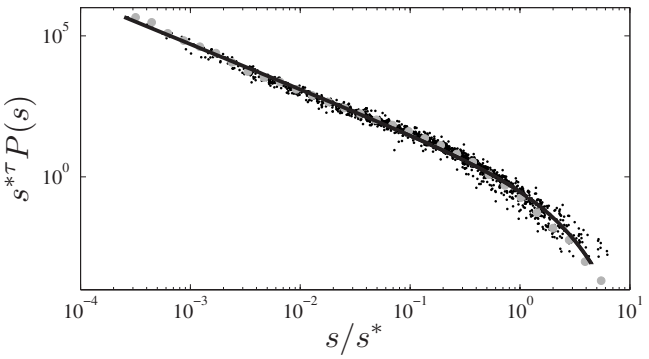

FIG. 6. Data collapse of the wetting cluster size distributions $P(s)$ extracted from the 139 simulations. The black dots show the individual data sets from all of the simulations, while the gray filled circles show the average extracted from them. The black solid line shows a function $\sim(s/s^*)^{-1.6}\exp(s/s^*)$, fitted to the full set of numerical data.

bolized ◇), the distributions become, with ascending graph number, more and more influenced by an exponential cutoff. From the limited statistics of these five data sets, arguably it may not be obvious that the leftmost graph (symbolized ○) is dominated by an exponential tail rather than a different power law. However, examining the full set of distributions we observe a similar trend, with a more gradual transition in the distribution behavior. This examination also indicates that the power law parameter τ takes approximately the same value in the distributions where a power law region is well defined. It was found that $\tau=1.60\pm0.10$. This is close to the value (1.70 ± 0.10) observed by Frette *et al.* in drainage processes with viscosity-matched fluids [43].

Now, assuming that all our distributions obey Eq. (16), we may consequently relate an s^* to each of them. The leftmost graph in the inset of Fig. 5, then being completely dominated by the exponential tail (symbolized ○), would have an s^* of the same order as the lower cutoff of the system. While similarly, the distribution where no exponential tail occurs at all (symbolized ◇), is expected to have an s^* larger than the upper cutoff given by the system size. Let us also assume that all our distributions would, had it not been for the lower cutoff given by the system, exhibit the same power law behavior. Then, Eq. (16) also predicts that a rescaling of the horizontal and vertical axis with $1/s^*$ and $s^{*\tau}$ respectively, will give a data collapse. We are here ultimately interested in how the flow and oscillatory stimulation parameters of the system affect its s^*. So instead of finding the cutoff cluster size for the individual cluster size distribution by numerically fitting it to the proposed distribution form of Eq. (16), we attempt to directly relate it to the physical flow parameters. By observing how well the distributions would collapse with different combinations of parameters we found from the results that, for a given density ratio and $\hat{F}_a \gg 1$, the cutoff size

$$s^* \propto \frac{\gamma^2}{a^2 T F_x}. \tag{17}$$

However, keeping all other parameters constant, varying the period of oscillations and the background body force independently, showed that, for the given parameter configuration, there exists a minimal cutoff cluster size that, in this high $\hat{F}_a$ regime, was inversely proportional to the amplitude of the oscillatory acceleration squared, and independent of the oscillation period and the background body force. To test for potential resolution effects, a limited set of simulations was produced. Here the system resolution, i.e., the number of lattice sites per solid disk in the porous medium, was quadrupled. These simulations confirmed the initially observed cutoff size dependence. Physically, s^* is related to the largest cluster size left in the system, and should mainly result from a balance of viscous, hydrostatic and capillary forces. In Sec. V, we show that this force balance produces a somewhat more complicated expression for s^* than that presented in Eq. (17). There we also give an interpretation of the observed TF_x dependency in the cutoff cluster size. Based on the full expression for s^* found in Sec. V, we have in the main graph of Fig. 5 obtained the data collapse of the five cluster size distributions, where we have used $\tau=1.6$.

In Fig. 6 the cluster size distributions of the full set of parameter variations are collapsed by the same proposed rescaling of the axes used in Fig. 5. This is observed to produce an excellent data collapse. The individual data sets are in the figure indicated by black dots. The gray filled circles show the average extracted from all of these sets. A power law behavior in a region over slightly more than three decades in s/s^* is observed in the collapsed data sets.

In a limited number of simulations we investigated the effect of applying the oscillatory stimulation of the system after an invasion stage of pure drainage had left the system saturated with invading fluid. In this set of simulations we varied the amplitude of the oscillatory body force only, leaving all other parameters constant. The fluids had a mass density ratio of 10^{-3}, $\mathrm{Ca}_x \approx 10^{-1}$ and $\hat{Q} \approx 2$, while $\hat{F}_a$ was varied from approximately 7 to 25. After introducing the oscillatory body force, stuck clusters in the predrained system were mobilized and propagated toward the outlet. The result was a decrease in the cutoff cluster size of the system. What we also saw was that this cutoff size was very close to, or equal to, that obtained by initiating the oscillatory stimulation at the beginning of the invasion process. The main graph of Fig. 7 shows exactly this. Here, the distributions represented by gray filled squares with black edges are extracted from simulations where an oscillatory body force was applied continuously from the start of the invasion process. The open black circles represent those where the system already had been drained before applying the same set of oscillatory stimulation. And the light gray squares represent the cluster distribution in the predrained system before oscillatory stimulation. From the figure the distributions that have the same stimulation parameters may easily be divided into pairs, since they to a large extent overlap. Thus, our results indicate that the effects of the oscillations are history independent. By that we mean that these effects are not strongly linked to the dynamical evolution of the system leading up to the final state of irreducible wetting fluid saturation. Assuming that any clusters larger than the cutoff cluster size s^*, given by the physical flow parameters, will be transported out of the porous cell during a transient state, it seems rea-

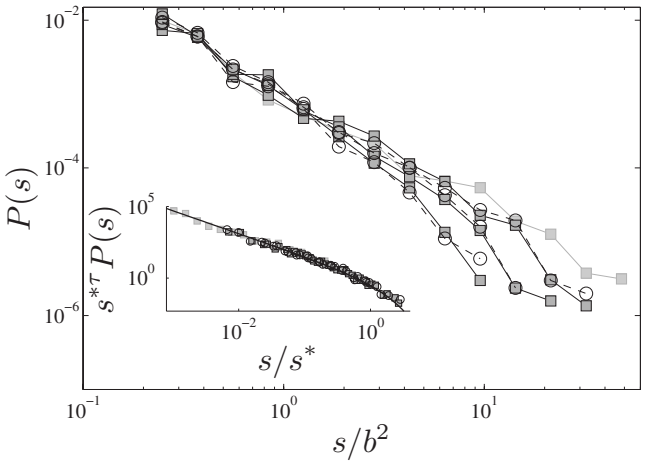

FIG. 7. Comparison between cluster size distributions achieved in systems pre-drained before subjecting them to oscillatory stimulation (open black circles) and distributions extracted from systems being continuously stimulated through the invasion process (gray filled squares with black edges). The light gray squares in the graphs represents the cluster distribution in the predrained system before oscillatory stimulation. The main graph shows the distributions $P(s)$ as functions of the cluster size divided by the pore length square. Solid lines connect the distributions from the continuously stimulated cases, while dashed lines connect the others. In the inset these distributions are rescaled in the same manner as in Figs. 5 and 6.

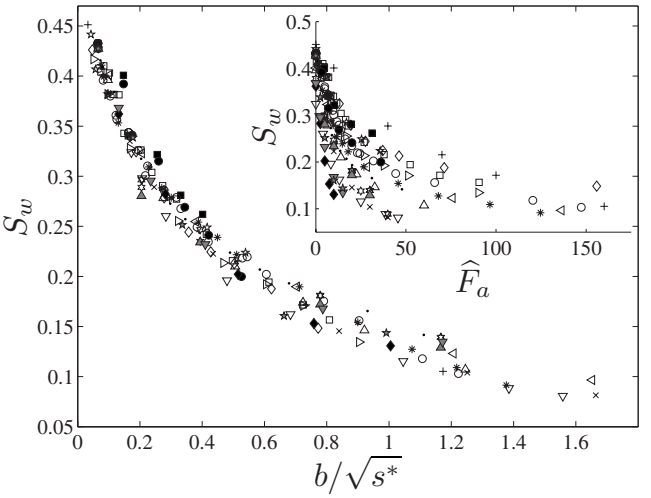

FIG. 8. The end saturation level S_w of the defending wetting fluid. In each of the data sets in the figure, indicated by the different symbols, all physical parameters except the acceleration amplitude a are kept constant. The main graph shows the end saturation plotted against the pore length b divided by the square root of cluster size s^*. The inset shows the end saturation as a function of the dimensionless $\hat{F}_a$.

sonable that an applied stimulation which should reduce the s^* of the system, results in a statistically specific cluster configuration, independent of the initial cluster configuration.

Thus far, we have discussed the effect the oscillatory body force has on the cutoff size in the cluster distribution in the system. But in the saturated state, and in a fluid extraction context, an obvious quantity of interest is the end saturation levels. How does the oscillatory acceleration of a porous medium affect the saturation levels? Figure 8 shows the end saturation in the simulations. Each simulation gives one data point on the graph. The inset displays the saturation of wetting clusters S_w plotted against the ratio $\hat{F}_a = \rho_w a / F_x$. In each data set all physical parameters except the acceleration amplitude a are kept constant. It is observed that the effect of the oscillatory body force amplitude on the system varies substantially depending on the rest of the physical parameters. If the saturation is, like in the main graph of Fig. 8, plotted against $b/\sqrt{s^*}$ instead, a well-defined function dependency is observed. This indicates that the end saturation is a function of the cutoff cluster size s^* alone. Given the total number of wetting clusters n_w left in the porous medium, the cluster size distribution, and the total pore space area A, the wetting fluid saturation is

$$S_w = \frac{n_w}{A}\langle s \rangle = \frac{n_w}{A}\int_{s_{\min}}^{s_{\max}} sP(s)ds. \tag{18}$$

The limits of integration $s_{\min}$ and $s_{\max}$ may here be taken to be 0 and ∞, respectively, since the integrand converges fast enough at these limits. Specifically, the integrand converges as approximately $s^{-0.6}$ in the lower limit and exponentially in the upper limit. If we assume that the number of wetting clusters n_w is a function of s^* only, and that we are in a regime where the exponent τ is constant, it is apparent from combining Eqs. (16) and (18) that the saturation should be dependent on one variable alone, the cutoff cluster size s^*. Since the number of wetting clusters is in the simulations observed to be a nontrivial function of s^*, and $\tau \approx 1.6$, these assumptions are found to be satisfied. From Fig. 8, we see immediately that the end saturation S_w of the defending fluid decreases with decreasing s^*. It is also observed that the largest rate of change in saturation is for the largest cutoff cluster sizes. This obviously means that in this region a small change in s^* leads to a relatively large change in S_w. It should here be noted that in the limit where s^* is much larger than the system size, the wetting saturation S_w is expected to depend on the system size itself. In the flow regime investigated here, however, the largest s^* encountered is of the same order as system size. Finite size effects are therefore not expected to be very pronounced in the scaling shown in Fig. 8.

From oil recovery point of view, a potentially substantial improvement in total recovery from an oil reservoir may be obtainable. Having in mind the results, shown in Fig. 7, from initiating stimulation late in the process, reservoirs showing signs of lowered oil production may also be revitalized by subjecting it to an oscillatory acceleration. The result of any oscillatory stimulation would then depend on how large a fraction of the initial oil has already been extracted from the reservoir.

V. THEORETICAL FOUNDATION FOR THE CUTOFF CLUSTER SIZE

To determine the effect the oscillatory stimulation has on the statistical cutoff cluster size s^*, it is useful to determine

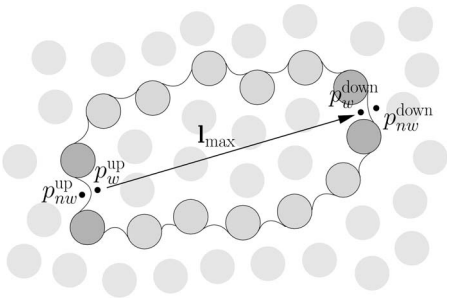

FIG. 9. Schematic representation of the pressure configuration in a stuck wetting cluster. Here only the two pores furthest upstream and downstream, separated by a length vector $\mathbf{l}_{\max}$, are considered. The pressure differences across the menisci of these two pores are then from the sketch given as $\Delta p^{\text{up}}=p_{nw}^{\text{up}}-p_w^{\text{up}}$ and $\Delta p^{\text{down}}=p_{nw}^{\text{down}}-p_w^{\text{down}}$.

the criterion for a fluid bubble/cluster to be mobilized in the porous medium. Let us now, as in the simulations, look at a wetting bubble, stuck in the pore space, surrounded by a nonwetting fluid. The pressure differences, $\Delta p(x,y)=p_{nw}(x,y)-p_w(x,y)$, across all the fluid interfaces of the wetting cluster are then balanced by the interface tension. Typically, to mobilize such a bubble the pressure differences across a pair of menisci must overcome the maximum capillary forces given by the local geometry of the pores in question. In a random, nearly homogeneous porous medium this pair of menisci would normally consist of the menisci in the furthest upstream and downstream pores [52] (see Fig. 9). The pressure balance across the menisci in a marginally stuck cluster, i.e., a cluster that will be mobilized by any additional forcing, would then be given by

$$\Delta p^{\text{up}} - \Delta p^{\text{down}} = \gamma\left(\frac{1}{R_{\text{cr}}^{\text{up}}} - \frac{1}{R_{\text{cr}}^{\text{down}}}\right) = \gamma\frac{C}{b}, \tag{19}$$

where C is a dimensionless parameter that relates the typical critical radii of curvature $R_{\text{cr}}^{\text{up}}$ and $R_{\text{cr}}^{\text{down}}$, for the upstream and downstream menisci respectively, to the diameter b of the disks constituting the porous medium. This parameter C contains the information of the typical local pore geometry, as well as the wetting properties of the fluids. Since we have investigated one porous medium only, and kept the wetting properties constant, C is taken to be a constant in this consideration. Rewriting the left hand side of Eq. (19) in terms of the pressure differences, $\Delta p_w=p_w^{\text{down}}-p_w^{\text{up}}$ and $\Delta p_{nw}=p_{nw}^{\text{down}}-p_{nw}^{\text{up}}$, between the downstream and upstream menisci positions in the two respective fluids (see Fig. 9), we get

$$\Delta p_w - \Delta p_{nw} = \gamma\frac{C}{b}. \tag{20}$$

In a system influenced by the body forces $F_x\mathbf{e}_x$ and a time independent $\rho a\mathbf{e}_y$, we have a hydrostatic pressure gradient $F_x\mathbf{e}_x+\rho_w a\mathbf{e}_y$ inside the stuck wetting bubble. This gives, inside the bubble, a pressure increase

$$\Delta p_w = (F_x\mathbf{e}_x + \rho_w a\mathbf{e}_y)\cdot\mathbf{l}_{\max}, \tag{21}$$

from the upstream meniscus to the downstream one. Here, $\mathbf{l}_{\max}$ is the length vector from the upstream meniscus to the downstream meniscus. In the surrounding nonwetting fluid the global average pressure gradient is from Darcy's law given as

$$(\nabla p_{nw})_{\text{global}} = F_x\mathbf{e}_x + \rho_{nw}a\mathbf{e}_y - \frac{\mu_{nw}}{\kappa_{nw}}\mathbf{u}_D, \tag{22}$$

where the last term on the right hand side is the average viscous contribution to the global average pressure gradient in the nonwetting fluid. Here, $\mathbf{u}_D$ is the Darcy velocity of the nonwetting fluid, μ_{nw} is its dynamical viscosity and κ_{nw} is, with respect to the nonwetting fluid, the effective permeability of the porous medium including stuck wetting bubbles. If the system is, as in our simulations, periodic in the y direction, the nonwetting fluid is allowed to flow under the influence of the described body forces. The viscous term in the global average pressure gradient then balances the other two terms perfectly. This leaves a vanishing global average pressure gradient. Locally, around the stuck wetting bubble under consideration, the situation is somewhat different. Here, the flow is typically different from the global average and this gives a local pressure increase upstream of the bubble and a decrease downstream. This is a result of the viscous drag from the stuck bubble. The pressure drop across the bubble may be estimated to be proportional to the bubble's length and the velocity far away from that bubble. The velocity far away from the bubble is again proportional to the Darcy velocity of the flowing nonwetting fluid. From Eq. (22) we observe that, when the global pressure gradient is vanishing, the Darcy velocity is proportional to the body forces influencing the flow of the nonwetting fluid. This gives

$$\Delta p_{nw} = -B(F_x\mathbf{e}_x + \rho_{nw}a\mathbf{e}_y)\cdot\mathbf{l}_{\max}. \tag{23}$$

The dimensionless B is the proportionality parameter that contains all the information about the viscous drag induced by the bubble. This is of course typically dependent of the size and shape of the bubble, as well as the configuration of the surrounding bubbles, since this influences the average flow far from the investigated bubble. This argument for the local pressure field around a stuck fluid cluster is similar to that presented by Amili and Yortsos [53]. Now, combining Eqs. (21) and (23) with Eq. (20) we have that

$$[(1+B)F_x\mathbf{e}_x + (\rho_w + B\rho_{nw})a\mathbf{e}_y]\cdot\mathbf{l}_{\max} = \gamma\frac{C}{b}. \tag{24}$$

Assuming that the two menisci in focus are situated such that the length vector $\mathbf{l}_{\max}$ aligns perfectly parallel to the vector $(1+B)F_x\mathbf{e}_x+(\rho_w+B\rho_{nw})a\mathbf{e}_y$, we may simplify the above equation, which gives us

$$l_{\max} = \frac{C\gamma}{[(1+B)^2F_x^2 + (\rho_w + B\rho_{nw})^2a^2]^{1/2}b}. \tag{25}$$

This expression for the length $l_{\max}$ across a marginally stuck bubble can be directly linked to the statistical cutoff size s^* of the system, introduced in Eq. (16), as long as clusters that exceed this maximal length are fragmented or transported out of the system. For this to hold in our system, F_x cannot be equal zero, since this is the only body force that contributes to any transport in the direction of the outlet. In agree-

ment with the simulations, a good assumption would be that $s^* \propto l_{\max}^2$. It was in these found that the clusters had a rather constant aspect ratio. They were, on average, twice as long as they were wide.

If we now look at a system where we have replaced the constant acceleration $a\mathbf{e}_y$, with one that oscillates with time in the same manner as in the simulations, the maximal size of a bubble that is trapped in the system changes. Exactly how this critical cluster length changes may not be obvious. However, there are some physical limits that may be to some help. For one, when the period of one transverse oscillation goes to zero the effect of the shaking should also go to zero. In the limit $T=0$ we then expect to have that $\Delta p_w - \Delta p_{nw} = (1+B)F_x l_{\max}$. This should obviously also be the case when the amplitude of the oscillatory acceleration $a=0$. Likewise, it is expected that as the period T becomes larger, the oscillatory body force affects the system more, and the cutoff cluster size becomes smaller. However, a reasonable assumption would be that, in our overdamped flow regime, the effect of the oscillatory acceleration, no matter how large a period, cannot be greater than the effect of a time independent acceleration of the same amplitude. There should therefore exist a lower limit for the obtainable cutoff cluster size. And this minimal cutoff size should be proportional to the expression in Eq. (25) squared. For larger T, but still small compared to the time to reach the state of irreducible saturation, it is expected that the cutoff cluster size approaches this minimal cutoff size.

To determine more specifically how the cutoff size is dependent on T, and any other physical parameters, we have to examine the results from the simulations. As described in Eq. (17), from the simulations we found that, for a given fluid density ratio and $\hat{F}_a \gg 1$, the statistical cutoff cluster size was inversely proportional to $a^2 T F_x$, as long as the product TF_x was smaller than some threshold value. If this product, on the other hand, was larger than the threshold value, the cutoff cluster size s^* was, in this high $\hat{F}_a$ regime, independent of the period T and the background body force F_x. This observed cutoff cluster size was identical, or close to identical, to the cutoff size produced in a system subjected to a constant time independent acceleration in the y direction, but otherwise given by the same parameter configuration.

This implies that the general expression for the statistical cutoff cluster size should be given as

$$s^* \propto \frac{\gamma^2 b^{-2}}{(1+B)^2 F_x^2 + (\rho_w + B\rho_{nw})^2 a^2 f(T,F_x)}, \tag{26}$$

where a function $f(T,F_x)$ has been introduced. Since this function has to be dimensionless, the construction

$$f(T,F_x) = \min\{\beta\hat{Q}, 1\}, \tag{27}$$

where $\hat{Q}$ was defined in Eq. (14), gives the desired function form. This function satisfies all the criteria given by theory and the simulation results. The $\beta\hat{Q}$ could then be interpreted as the average number of pores a mobile cluster can propagate through in the direction of the outlet, in half a period of oscillations. Here, β is a dimensionless proportionality factor that presumably is related to the effects of the two-phase flow. Further investigation showed that if clusters could propagate a distance of more than one pore on average, in the direction of the outlet, in half a period, the result was a cutoff cluster size where $f(T,F_x)=1$. This would essentially mean that if a cluster meniscus can propagate a distance of at least one whole pore, toward the outlet, in half a period, the effect is equal to that of a constant time independent acceleration. In this case, a cluster's propagation toward the outlet may be regarded as irreversible. The cluster is then never in the same set of pores for more than half a period, and is allowed to probe new sets of pores each time the acceleration direction changes. This access to only new pores is similar to the situation having a time independent acceleration. Thus, it seems reasonable that these two processes have the same cluster size behavior. If the cluster, on the other hand, is unable to move a whole pore length toward the outlet, the effect of the oscillatory acceleration amplitude is reduced. This is realized in Eq. (26) where the second term of the denominator is reduced by a factor equal the average length the cluster is able to propagate toward the outlet, relative to one pore length. In this regime, the menisci probe on average a set of pores more than once. But even though a meniscus may on average not be able to propagate through a whole pore toward the outlet, the movement could still initiate coalescence of neighboring clusters and therefore give a statistical cutoff cluster size different from that observed in systems subjected to a background body force F_x alone. The factor $\beta\hat{Q}$ may therefore perhaps also indicate the statistical range of coalescence in the direction of the outlet. Clusters that move a shorter distance than this in half a cycle are effectively stuck in the porous medium because they are not able to coalesce with other clusters. And therefore the statistical cutoff cluster size s^* is modified by this factor.

By expressing the cutoff cluster size in the dimensionless numbers presented in Sec. IV, we get

$$s^* \propto \frac{b^2 \mathrm{Ca}_x^{-2}}{(1+B)^2 + \min\{\beta\hat{Q}, 1\}\left(1 + B\frac{\rho_{nw}}{\rho_w}\right)^2 \hat{F}_a^2}. \tag{28}$$

The two parameters B and β introduced in this argument are taken to be free tuning constants, since a more focused investigation of their behavior would otherwise be necessary. These parameters were in our simulations approximated to be $B=0.7$ and $\beta=0.15$, based on how good a data collapse they produced. With these given values of B and β all the data collapses in Sec. IV B were produced.

VI. CONCLUSION

Motivated by seismic stimulation as a possible method for enhanced oil recovery, we have in this paper numerically studied the statistical effects of transverse oscillatory acceleration of a porous medium during a drainage process. In the investigation we used a 2D lattice Boltzmann algorithm to simulate a system consisting of approximately 60×30 pores. This system was large enough to obtain cluster statistics for the defending fluid. The viscosity difference between the two

fluids was small, having a viscosity ratio $M=0.2$. The study mainly focused on how flow and oscillatory stimulation parameters affected the resulting cluster configurations in a state of irreducible saturation. It was observed that in this state, the cluster size distributions followed a power law with an exponential tail. The power law exponent was approximated to be $\tau \approx 1.6$. Based on theoretical arguments, an analytical expression for the cutoff cluster size s^* of the distribution was found. Specifically, it was found that this cutoff size is strongly coupled to the amplitude of the oscillatory acceleration of the system. A larger acceleration amplitude led to a smaller cutoff size in the system. The oscillation period, on the other hand, only influenced the cutoff size up to some threshold. Below this threshold, a larger oscillation period gave a smaller cutoff size. The cutoff cluster size was also shown to control the end saturation S_w of the defending fluid. A smaller s^* gave a lower S_w. Because of these relations it is possible to predict changes in saturation, given changes in the physical parameters.

A limited set of simulations, where the stimulation was applied only after a stage of pure drainage had left the system in a stationary state, also showed that the resulting cluster configurations were statistically the same as when applying stimulation during the whole invasion process. This indicated that the resulting cluster structures are not strongly history dependent. However, here a more thorough investigation is needed. In the flow regime investigated in this study, the oscillatory stimulations always proved to give an increase in the total amount of defending fluid extracted from the porous medium.

ACKNOWLEDGMENTS

The work was supported by The Norwegian Research Council, through PETROMAKS. A special thanks to Steven R. Pride and Renaud Toussaint for many useful discussions. Thanks to Ken Tore Tallakstad for assistance in the data analysis and for many useful comments.

[1] I. A. Beresnev and P. A. Johnson, Geophysics **59**, 1000 (1994).
[2] M. Hilpert, G. H. Jirka, and E. J. Plate, Geophysics **65**, 874 (2000).
[3] D. R. Graham and J. J. L. Higdon, J. Fluid Mech. **425**, 55 (2000).
[4] P. P. Iassonov and I. A. Beresnev, J. Geophys. Res. **108**, 2138 (2003).
[5] P. P. Iassonov and I. A. Beresnev, SPE J. **13**, 465 (2008).
[6] I. A. Beresnev, Geophysics **71**, N47 (2006).
[7] M. Hilpert, J. Colloid Interface Sci. **309**, 493 (2007).
[8] M. A. Biot, J. Acoust. Soc. Am. **28**, 168 (1956).
[9] M. A. Biot, J. Acoust. Soc. Am. **28**, 179 (1956).
[10] M. A. Biot, J. Acoust. Soc. Am. **34**, 1254 (1962).
[11] S. R. Pride, E. G. Flekkøy, and O. Aursjø, Geophysics **73**, O23 (2008).
[12] L. N. Reddi and S. Challa, J. Environ. Eng. **120**, 1170 (1994).
[13] L. N. Reddi and H. Wu, J. Environ. Eng. **122**, 1115 (1996).
[14] P. M. Roberts, A. Sharma, V. Uddameri, M. Monagle, D. E. Dale, and L. K. Steck, Environ. Eng. Sci. **18**, 67 (2001).
[15] I. A. Beresnev, R. D. Vigil, W. Li, W. D. Pennington, R. M. Turpening, P. P. Iassonov, and R. P. Ewing, Geophys. Res. Lett. **32**, L13303 (2005).
[16] W. Li, R. D. Vigil, I. A. Beresnev, P. Iassonov, and R. Ewing, J. Colloid Interface Sci. **289**, 193 (2005).
[17] U. Frisch, D. d'Humières, B. Hasslacher, P. Lallemand, Y. Pomeau, and J.-P. Rivet, Complex Syst. **1**, 649 (1987).
[18] A. K. Gunstensen, D. H. Rothman, S. Zaleski, and G. Zanetti, Phys. Rev. A **43**, 4320 (1991).
[19] A. K. Gunstensen and D. H. Rothman, J. Geophys. Res. **98**, 6431 (1993).
[20] D. Rothman and S. Zaleski, *Lattice-Gas Cellular Automata: Simple Models of Complex Hydrodynamics* (Cambridge University Press, Cambridge, England, 1997).
[21] F. A. L. Dullien, *Porous Media Fluid Transport and Pore Structure*, 2nd ed. (Academic Press, San Diego, 1992).
[22] M. Sahimi, *Flow and Transport in Porous Media and Fractured Rock* (VCH Verlagsgesellschaft mbH, Weinheim, 1995).
[23] J. Bear, *Dynamics of Fluids in Porous Media* (American Elsevier, New York, 1972).
[24] R. Lenormand, E. Touboul, and C. Zarcone, J. Fluid Mech. **189**, 165 (1988).
[25] P. G. Saffman and G. Taylor, Proc. R. Soc. London, Ser. A **245**, 312 (1958).
[26] M. Sahimi, Rev. Mod. Phys. **65**, 1393 (1993).
[27] R. Lenormand and C. Zarcone, Transp. Porous Media **4**, 599 (1989).
[28] K. T. Tallakstad, H. A. Knudsen, T. Ramstad, G. Løvoll, K. J. Måløy, R. Toussaint, and E. G. Flekkøy, Phys. Rev. Lett. **102**, 074502 (2009).
[29] K. T. Tallakstad, G. Løvoll, H. A. Knudsen, T. Ramstad, E. G. Flekkøy, and K. J. Måløy, Phys. Rev. E **80**, 036308 (2009).
[30] H. A. Knudsen and A. Hansen, Phys. Rev. E **65**, 056310 (2002).
[31] H. A. Knudsen and A. Hansen, Eur. Phys. J. B **49**, 109 (2006).
[32] T. Ramstad and A. Hansen, Phys. Rev. E **73**, 026306 (2006).
[33] R. Lenormand, Proc. R. Soc. London, Ser. A **423**, 159 (1989).
[34] R. Lenormand and C. Zarcone, Phys. Rev. Lett. **54**, 2226 (1985).
[35] D. Wilkinson and J. F. Willemsen, J. Phys. A **16**, 3365 (1983).
[36] M. M. Dias and D. Wilkinson, J. Phys. A **19**, 3131 (1986).
[37] P. Meakin, Physica A **173**, 305 (1991).
[38] L. Paterson, Phys. Rev. Lett. **52**, 1621 (1984).
[39] G. Løvoll, Y. Méheust, R. Toussaint, J. Schmittbuhl, and K. J. Måløy, Phys. Rev. E **70**, 026301 (2004).
[40] K. J. Måløy, J. Feder, and T. Jøssang, Phys. Rev. Lett. **55**, 2688 (1985).
[41] J. P. Stokes, D. A. Weitz, J. P. Gollub, A. Dougherty, M. O. Robbins, P. M. Chaikin, and H. M. Lindsay, Phys. Rev. Lett. **57**, 1718 (1986).
[42] D. A. Weitz, J. P. Stokes, R. C. Ball, and A. P. Kushnick, Phys. Rev. Lett. **59**, 2967 (1987).
[43] O. I. Frette, K. J. Måløy, J. Schmittbuhl, and A. Hansen, Phys.

Rev. E **55**, 2969 (1997).
[44] Y. Méheust, G. Løvoll, K. J. Måløy, and J. Schmittbuhl, Phys. Rev. E **66**, 051603 (2002).
[45] P. R. King, J. Phys. A **20**, L529 (1987).
[46] M. Ferer, W. N. Sams, R. A. Geisbrecht, and D. H. Smith, Phys. Rev. E **47**, 2713 (1993).
[47] V. Frette, J. Feder, T. Jøssang, P. Meakin, and K. J. Måløy, Phys. Rev. E **50**, 2881 (1994).
[48] M. Latva-Kokko and D. H. Rothman, Phys. Rev. E **72**, 046701 (2005).
[49] S. Succi, E. Foti, and F. Higuera, EPL **10**, 433 (1989).
[50] L. D. Landau and E. M. Lifshitz, *Fluid Mechanics*, 2nd ed. (Elsevier, London, 1989).
[51] D. Stauffer and A. Aharony, *Introduction to Percolation Theory* (Taylor & Francis, London, 1992).
[52] H. Auradou, K. J. Måløy, J. Schmittbuhl, and A. Hansen, Transp. Porous Media **50**, 267 (2003).
[53] P. Amili and Y. C. Yortsos, Transp. Porous Media **64**, 25 (2006).